Fabrication of GaN/Diamond Heterointerface and Interfacial Chemical Bonding State for Highly Efficient Device Design

Jianbo Liang, Ayaka Kobayashi, Yasuo Shimizu, Yutaka Ohno, Seong-Woo Kim, Koji Koyama, Makoto Kasu, Yasuyoshi Nagai, Naoteru Shigekawa

Highlights	・これまで不可能とされていた窒化ガリウム（GaN）とダイヤモンドの直接接合に成功。 ・1,000℃の熱を加えても耐え得る、安定した接合であることを実証。 ・従来より冷却が容易になり、大幅な省エネが実現できるため、持続可能な社会の貢献にも寄与。 ・直接接合により壊れたダイヤモンドの結晶構造を熱処理すると再結晶化することが明らかに。
概　要	研究グループは、窒化ガリウムとダイヤモンドの直接接合に成功しました。 窒化ガリウムを利用したトランジスタは、シリコンに代わる次世代半導体として、携帯電話の基地局などで幅広く使用されているものの、動作時に極度に温度上昇するため性能が大きく制限されています。加えて大型の放熱部材も必要です。 梁准教授らの研究グループは、地球上で最も熱伝導率が高く、最も効率的に熱を逃すことができるダイヤモンドと窒化ガリウムとの常温での直接接合に成功し、直接接合が 1,000℃の熱処理にも耐えることを実証しました。更に、接合に際してダイヤモンドの結晶構造が壊れるものの、熱処理することで再結晶化することを明らかにしました。これは界面で高い熱伝導率が保持することを示します。今回の成果により窒化ガリウムトランジスタで発生する温度上昇をこれまでの 1/4 倍程度まで抑制でき、大幅な省エネにつながると予測されます。今後、窒化ガリウムトランジスタの使用範囲が拡大し、レーダーやインバータなどの大電力用途にも使用できるとともに、持続可能な社会の実現にも貢献すると期待されます。 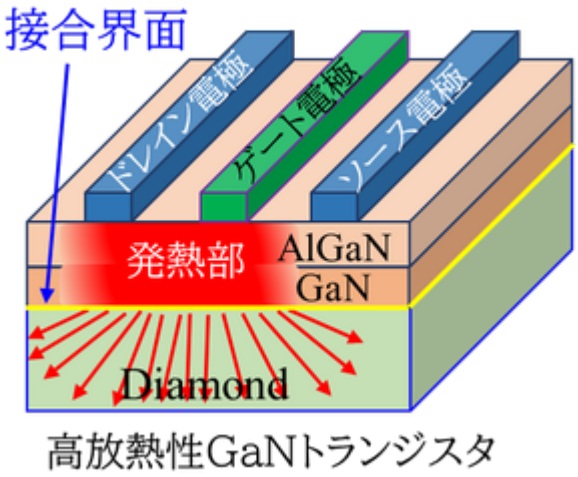 高放熱性GaNトランジスタ 'LED 照明などで広く活用されている窒化ガリウムとダイヤモンドの直接接合に世界で初めて成功'. 大阪市立大学. https://www.osaka-cu.ac.jp/ja/news/2021/210909. (参照 2021-09-09)

Liang, J., Kobayashi, A., Shimizu, Y., Ohno, Y., Kim, S., Koyama, K., Kasu, M., Nagai, Y., & Shigekawa, N. (2021). Fabrication of GaN/Diamond Heterointerface and Interfacial Chemical Bonding State for Highly Efficient Device Design. *Advanced Materials*, 33. 42104564. https://doi.org/10.1002/adma.202104564

Fabrication of GaN/Diamond Heterointerface and Interfacial Chemical Bonding State for Highly Efficient Device Design

Jianbo Liang, Ayaka Kobayashi, Yasuo Shimizu, Yutaka Ohno, Seong-Woo Kim, Koji Koyama, Makoto Kasu, Yasuyoshi Nagai, and Naoteru Shigekawa*

Dr. J. B Liang, Miss A. Kobayashi, Prof. N. Shigekawa

Department of Electronic Information Systems, Osaka City University, 3-3-138 Sugimoto, Sumiyoshi-Ku, Osaka 558 – 8585, Japan

E-mail: liang@osaka-cu.ac.jp

Dr. Y. Shimizu

Institute for Materials Research (IMR), Tohoku University, 2145-2 Narita, Oarai, Ibaraki 311–1313, Japan (Present address: National Institute for Materials Science, 1-2-1 Sengen, Tsukuba, Ibaraki 305–0047, Japan)

Prof. Y. Ohno

Institute for Materials Research (IMR), Tohoku University, 2-1-1 Katahira, Sendai 980–8577, Japan

Dr. S. Kim, Dr. K. Koyama

Adamant Namiki Precision Jewel. Co., Ltd, 3-8-22 Shinden, Adachi-ku, Tokyo 123–8511, Japan

Prof. M. Kasu

Department of Electrical and Electronic Engineering, Saga University, 1 Honjo-machi, Saga 840–8502, Japan

Prof. Y. Nagai

Institute for Materials Research (IMR), Tohoku University, 2145-2 Narita, Oarai, Ibaraki 311–1313, Japan

Keywords: GaN/diamond heterointerface, residual stress, sp^2 ratio, intensity gradients, surface activated bonding.

The intensity gradients for C, Ga, and N atoms become more abrupt with the reduction of the intermediate layer thickness. Diffusion of the C atom into the GaN adjacent to the heterointerface is observed, with the C atom acting as a dopant that compensates for the nitrogen vacancies in the GaN to increase the breakdown voltage.

1. **Introduction**

Diamond is one of the most promising candidates as a next-generation semiconductor material for high-output and low-loss power devices thanks to its superior material properties such as ultra-wide band gap, high carrier mobility,[1] high saturation velocity,[2] high chemical inertness, and the highest electrical breakdown field strength.[3] Accordingly, the figures of merit for high-power, high-frequency, and low-loss devices are extremely high.[4] Furthermore, diamond possesses the highest thermal conductivity among known materials and is the most promising material for a superior heat-spreading substrate for power devices. Unfortunately, *n*-type doping diamond with a sufficiently high electron conductivity has not yet been realized. Phosphorus (P) and nitrogen (N) are currently used for *n*-type diamond dopants, and the doped diamond exhibits a deep impurity level that makes it very difficult to activate at room temperature. Hence, the lack of an efficient *n*-type doping diamond limits its application range. The reverse doping issue exists in other wide-band-gap materials like GaN or AlGaN. *p*-type doping of GaN with a high Mg content has been very difficult so far. If the properties of diamond and GaN could be combined, it would be possible to overcome their doping bottleneck.

GaN-based devices have been extensively studied for high-frequency and high-power applications. Thermal management remains an important technical issue that is limiting device performance and reliability. Diamond as a promising heat-spreading substrate is being extensively studied in GaN-based devices.[5-9] A GaN-on-diamond structure has been developed by either removing Si from the GaN-on-Si substrate and depositing diamond on the exposed GaN surface using a dielectric material transition layer such as SiN_x or AlN[10-12], or removing Si from the GaN-on-Si substrate and bonding it to a diamond substrate using an adhesion layer such as metal or amorphous Si.[13-16] For the former, the transition layer contributes to a large thermal resistance between GaN and diamond, and the thermal conductivity of the deposited diamond is very low due to a low crystal quality, which prevents the desired thermal management from being achieved. For the latter case, the use of the adhesion material with poor thermal conductivity will substantially raise the thermal boundary resistance (TBR) between GaN and diamond, and a parasitic capacitance will be generated in the devices during high-frequency operation due to the low electrical resistivity of the adhesion material. There is thus

a need for a technology that can directly integrate diamond and GaN. However, due to large differences in their crystal structures and lattice constants, direct diamond growth on GaN and vice versa is impossible.

One way to overcome the lattice and thermal expansion mismatches between the integrating substrates is wafer direct bonding. Recently, Ga_2O_3/diamond,[17] Si/diamond,[18] InGaP/diamond,[19] and GaN/Si.[20] heterougensou intetrations using low-temperature hydrophilic bonding or plasma activation bonding method have been demonstrated. Althouth the direct bonding of diamond and dissimilar materials can be achieved at low-temperatures, the thermal stability of the bonding interface is very concerned. For direct bonding method such as hydrophilic, hydrophobic, and plasma-assisted bondings, a post-annealing process is essential for achieving high bonding strenth. However, high annealing temperature (typically > 500 °C) generally causes cracks of the bonded sample or exfoliation of the bonded interface due to a large thermal expansion coefficient mismatch. The poor thermal stability severely limits the application of wafer direct bonding technology. On the other hand, surface activated bonding (SAB) method, in which a direc bonding of dissimilar materrials with high bonding strenght can be achieved after activating the bonding material surface by an argon fast atom beam irradiation at room temperature. We have previously explored and successfully demonstrated the fabrication of Si/diamond[21,22] and GaAs/diamond[23] heterointerfaces at room temperature through SAB method and found that an amorphous layer with a thickness of several nanometers was formed at the heterointerfaces. Moreover, the heterointerfaces exhibited a high thermal stability and an excellent practicality.

In this work, we explore the fabrication of a GaN/diamond heterointerface using SAB method at room temperature and remove the amorphous layer formed at the heterointerface. GaN is completely different from InGaP, Si, and GaAs in material and chemical properties, which makes it very difficult to atomically clean and activate, as well as to get an atomic smooth surface. Therefore, how to achieve the direct bonding of GaN and diamond is a huge challenge. To examine this, we tested the thermal stability of the heterointerface at 700 °C in N_2 gas ambient pressure, which is required for GaN-based power device fabrication processes. The residual stress in the GaN of the heterointerface was characterized by micro-Raman spectroscopy. The nanostructure and the atomic behavior of the heterointerface were systematically investigated by transmission electron microscopy (TEM) and energy-dispersive X-ray spectroscopy. The chemical bonding states of the carbon atoms at the heterointerface were also investigated by electron energy-loss spectroscopy (EELS).

2. **Results and discussion**

A schematic cross-section and a low-magnification cross-sectional TEM image of the GaN/diamond bonded sample are shown in Figure 1(a) and (b), respectively. The thicknesses of the GaN layer and the buffer layer grown on Si were determined to be 1080 and 122 nm, respectively. An optical microscope image of the GaN layer bonded to the diamond after removing the Si substrate is shown in Figure 1(c). About 90 % bonded area was obtained. A part of the GaN layer bonded to diamond was exfoliated, which is attributed to the point defects formed on the surface of GaN epitaxial layer formed on Si prior to bonding (see Figure S1). In addition, the unbonded area was located on the edge of the diamond surface, which resulted from the mechanical polishing damage during the Si substrate removal process. After annealing at 700 °C for 60 s in N_2 atmosphere, no reduction in the bonded area was observed in the 700 °C-annealed GaN/diamond bonded sample, as shown in Figure 1(d). On the other hand, although some buffer layer dissolved regions were observed on the surface of the GaN/diamond bonded sample after annealing at 1000 °C (see Figure S2(a) and (b) in the supplementary materials), no bonding interface peeling was observed. These results indicate that the GaN/diamond heterointerface can withstand the harsh fabrications processes GaN-based power devices are subjected to, such as high-temperature treatment for forming ohmic contacts.

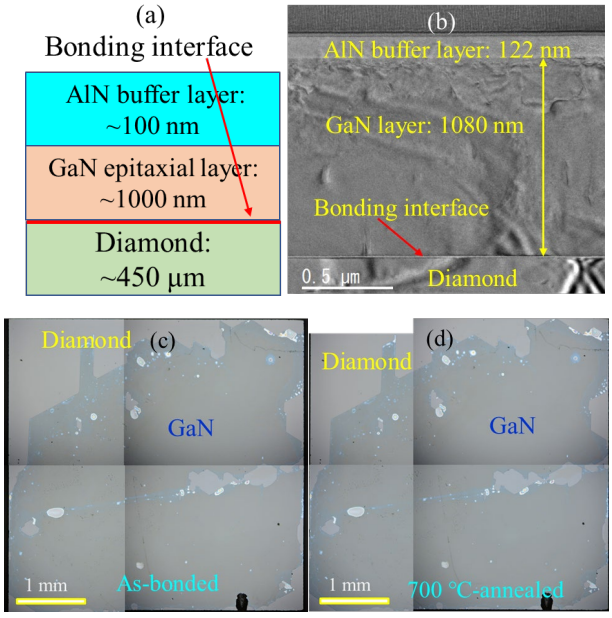

Figure 1. (a) Schematic cross-section and (b) low-magnification cross-sectional TEM image of GaN/diamond bonding sample. Optical microscope images of (c) as-bonded GaN/diamond sample and (d) 700 °C-annealed GaN/diamond sample.

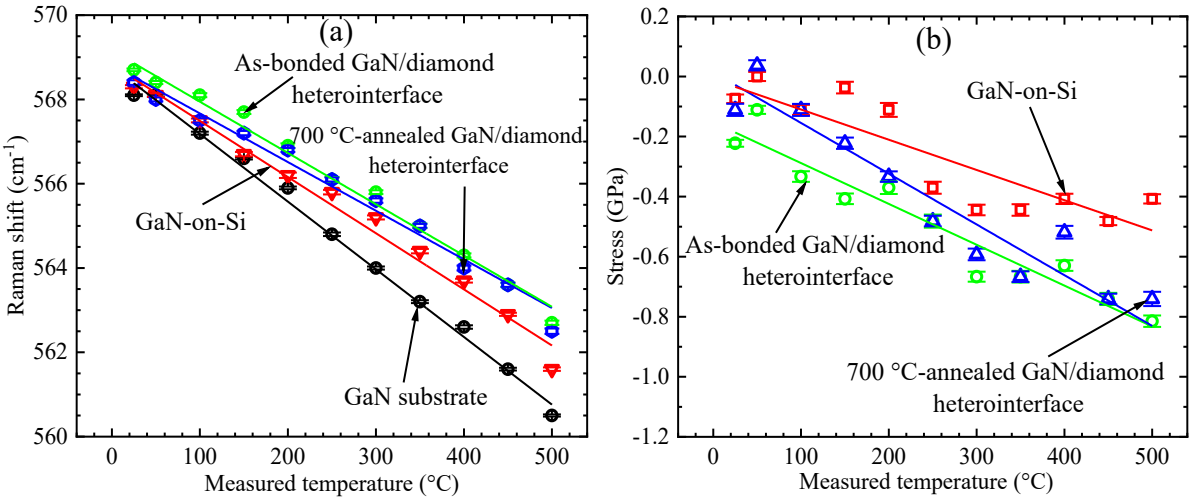

Figure 2. (a) Raman shift of GaN in a stress-free GaN substrate, GaN layer grown on Si substrate, the as-bonded and 700 °C-annealed GaN/diamond heterointerfaces and (b) biaxial stress in the GaN layers grown on Si, the as-bonded and 700 °C-annealed GaN/diamond heterointerfaces as a function of measured temperature. Negative sign indicates a compressive stress. The phonon frequency shift contributing to measured temperature was subtracted after comparison with a calibration performed on a stress-free GaN substrate.

The Raman peak shift and the biaxial stress of GaN E_2 -high mode in a stress-free GaN substrate, GaN layer grown on Si substrate, and the as-bonded and the 700 °C-annealed GaN/diamond heterointerfaces as a function of measured temperatures are shown in Figure 2(a) and (b), respectively. We can see that the GaN phonon frequency linearly shifted with a residual stress of 2.7 cm^{-1} GPa^{-1}.[24] The values of the biaxial stress in the GaN grown on the Si substrate and the as-bonded and 700 °C-annealed GaN/diamond heterointerfaces were calculated with respect to the stress-free GaN substrate. For the stress-free GaN, the Raman peak shift of GaN E_2 -high mode is widely varied, as shown in Table I. GaN grown by Hydride Vapor Phase Epitaxy (HVPE) method showed a small variation in the Raman peak shift, the Raman peak position of GaN E_2 -high mode was found to be the closest the theoreticaly calculated Raman peak position. Thus, we adopted a *c*-plane (0001) GaN single-crystal substrate grown by HVPE as the stress-free GaN that was provided by Sciocs Co., Ltd. The Raman peak of the stress-free GaN substrate was observed at 568.1 cm^{-1}.

Table I. Phonon frequency in wurtzite GaN obtained by Raman spectroscopy at 300K

Type	Method	E_2-high [cm^{-1}]
GaN	Calculation	579.0[25]
GaN	HVPE	568.0[26]
GaN	HVPE	567.2~568.1[27]

GaN/sapphire	HVPE	568.0[28]
GaN/Si(111)	Metalorganic Chemical Vapor Deposition (MOCVD)	566.2~566.8[29]
GaN/SiC	HVPE	568.0[30]

The Raman peak in the GaN grown on Si and the as-bonded and 700 °C-annealed GaN/diamond heterointerfaces exhibited shifts to lower wave numbers compared to the stress-free GaN substrate at room temperature. In addition, the Raman peak shifts to lower wave numbers with increasing measured temperature. The Raman peak shift in the as-bonded GaN/diamond heterointerface was significantly larger than that of the GaN grown on Si. On the other hand, the Raman peak shift in the 700 °C-annealed GaN/diamond heterointerface was smaller than that of the as-bonded GaN/diamond heterointerface when the temperature was lower than 200 °C. The phonon frequency shift contributing to the measured temperature was subtracted from the stress-free GaN substrate. At room temperature, there was a compressive stress of 0.07, 0.22, and 0.1 GPa in the GaN grown on Si, the as-bonded, and the 700 °C-annealed GaN/diamond heterointerfaces, respectively, which increased to 0.41, 0.81, and 0.74 GPa at 500 °C, i.e., higher than the typical operation temperature of GaN-based devices.

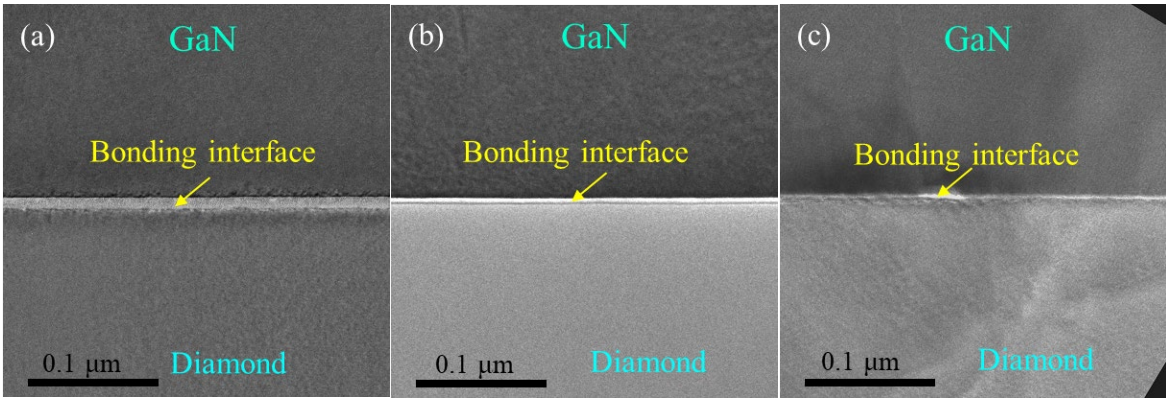

Figure 3. Cross-sectional low-magnification TEM images of (a) as-bonded, (b) 700 °C-annealed, and (c) 1000°C-annealed GaN/diamond heterointerfaces.

Figure 3(a)–(c) shows cross-sectional low magnification TEM images of as-bonded, 700 °C-annealed, and 1000 °C-annealed GaN/diamond heterointerfaces, respectively. A thin intermediate layer located at the center of the TEM images can be observed, which corresponds to the bonding heterointerface. The thickness of the intermediate layer formed at the heterointerface obviously decreased with increasing annealing temperature. Peeling of the bonding interface and mechanical defects were not observed near the bonding heterointerface

even after annealing at 700 and 1000 ℃. These results demonstrate that the GaN/diamond heterointerface has excellent thermal stability up to 1000 ℃.

Figure 4(a) and (b) shows high-resolution TEM (HRTEM) images taken along the GaN [$1\bar{1}00$] and diamond [001] zone axes of an as-bonded GaN/diamond heterointerface, respectively. No lattice fringes were observed in the intermediate layer, and the thickness was measured to be approximately 5.3 nm. EDS mappings of the as-bonded GaN/diamond heterointerface are shown in Figure 4(c). EDS in the as-bonded GaN/diamond heterointerface revealed a steep heterointerface. When we compare the EDX mappings, it is clear that an oxide layer and a carbon transition layer were formed at the heterointerface. The X-ray intensity profiles for the C, Ga, O, and N atoms (highlighted in red, blue, cyan, and green, respectively) across the as-bonded GaN/diamond heterointerface are shown in Figure 4(d). The inset TEM image back indicates the corresponding location of the measured X-ray intensity profiles. Intensity gradients for the C, GaN, and N atoms were observed in the intermediate layer, and the intensity gradient of the C atoms showed a ladder distribution. In addition, a small peak for the intensity profile of the O atoms was observed, which we attribute to the residual oxygen of the vacuum system.

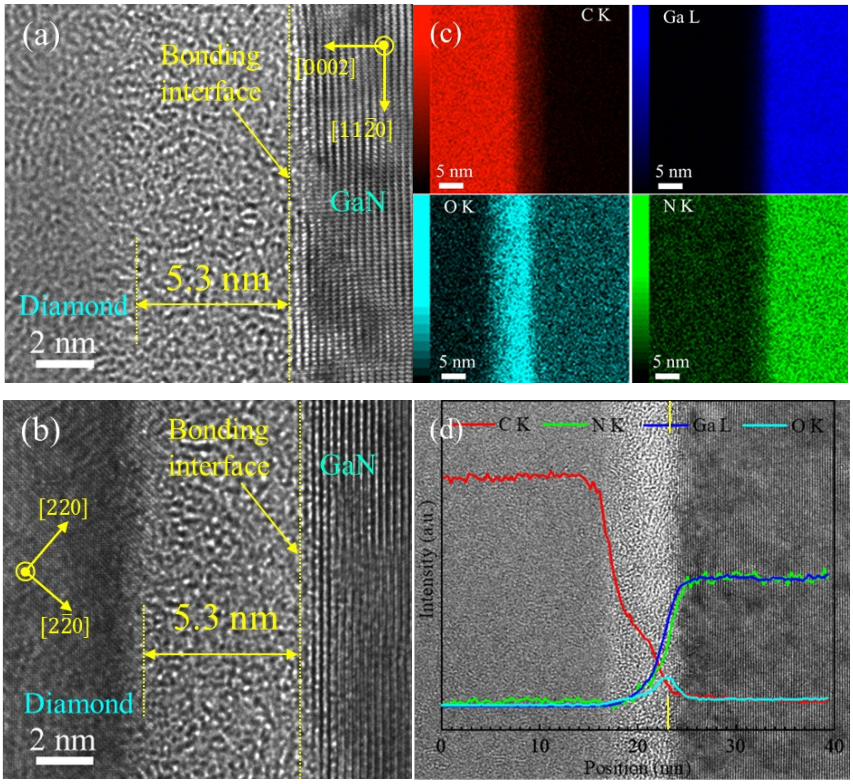

Figure 4. HRTEM images taken along (a) GaN [$1\bar{1}00$] zone axis and (b) diamond [001] zone axis on as-bonded GaN/diamond heterointerface. (c) EDS mappings of the heterointerface. (d) X-ray intensity profiles for C, Ga, O, and N atoms (red, blue, cyan, and green, respectively)

across the heterointerface. The inset TEM image back in (d) indicates the corresponding location of the measured X-ray intensity profiles for C, N, Ga, and O atoms.

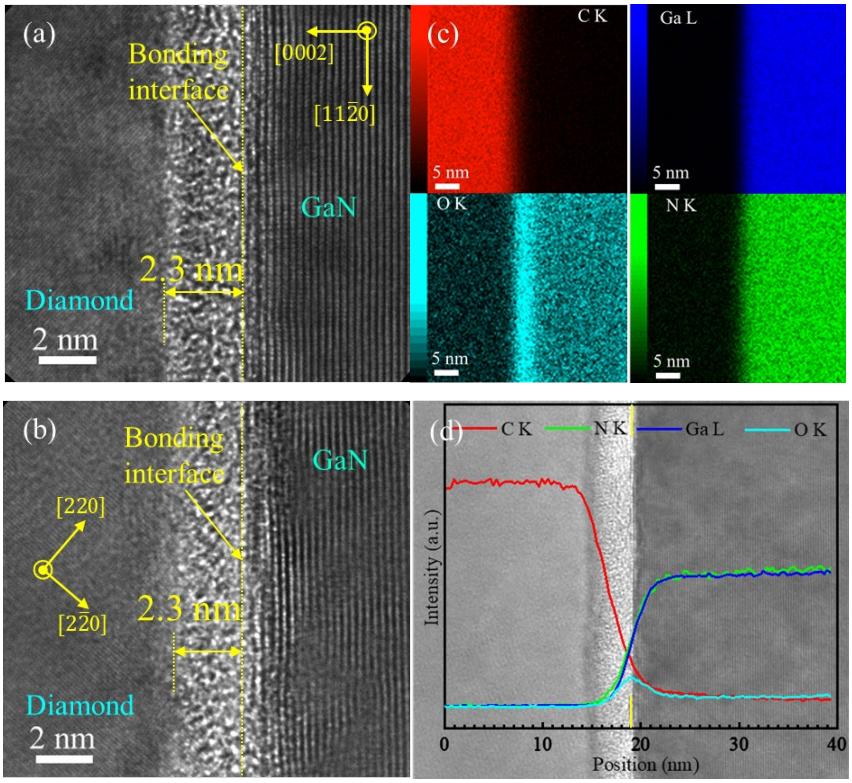

Figure 5. HRTEM images taken along (a) GaN [1$\bar{1}$00] zone axis and (b) diamond [001] zone axis of a 700 ℃-annealed GaN/diamond heterointerface. (c) EDS mappings of the heterointerface. (d) X-ray intensity profiles for C, Ga, O, and N atoms (red, blue, cyan, and green, respectively) across the heterointerface. The inset TEM image back in (d) indicates the corresponding location of the measured X-ray intensity profiles for C, N, Ga, and O atoms.

HRTEM images taken along the GaN [1$\bar{1}$00] and diamond [001] zone axes of the 700 ℃-annealed GaN/diamond heterointerface, EDS mappings of the heterointerface, and X-ray intensity profiles for the C, Ga, O, and N atoms across the heterointerface are shown in Figure 5(a)–(d). We can clearly see that the thickness of the intermediate layer decreased from 5.3 to 2.3 nm. The full width at half maximum (FWHM) of the intensity profile for O atoms became larger and the intensity gradients for the C, Ga, and N atoms became more abrupt in the intermediate layer, as shown in Figure 5(d). In addition, we can see that C atoms diffused into the GaN substrate adjacent to the intermediate layer.

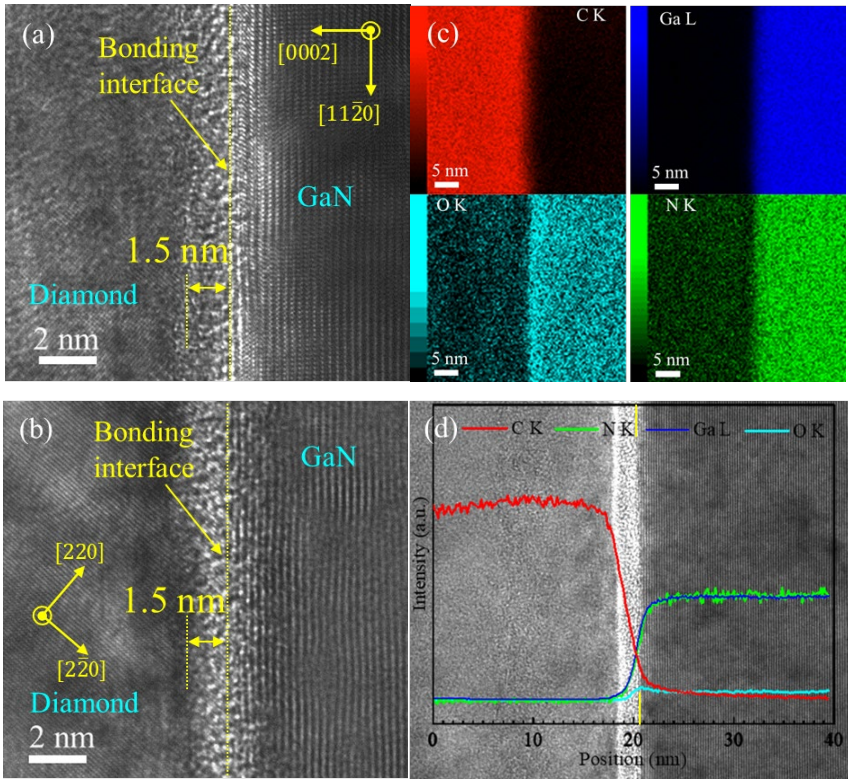

Figure 6. HRTEM images taken along (a) GaN [1$\bar{1}$00] zone axis and (b) diamond [001] zone axis of a 1000 °C-annealed GaN/diamond heterointerface. (c) EDS mappings of the heterointerface. (d) X-ray intensity profiles for C, Ga, O, and N atoms (red, blue, cyan, and green, respectively) across the heterointerface. The inset TEM image back in (d) indicates the corresponding location of the measured X-ray intensity profiles for C, N, Ga, and O atoms.

Figure 6(a)–(d) shows high-resolution TEM (HRTEM) images taken along the GaN [1$\bar{1}$00] and diamond [001] zone axes of a 1000 °C-annealed GaN/diamond heterointerface, EDS mappings of the heterointerface, and the X-ray intensity profiles for the C, Ga, O, and N atoms across the heterointerface. We can see that the intermediate layer thickness was further decreased by 1.5 nm. Lattice fringes were observed in the intermediate layer, which correspond to the diamond (220) plane. The C atoms further diffused into the GaN substrate adjacent to the intermediate layer with increasing annealing temperature, which caused the O atoms distributed in the intermediate layer to decrease. The diffusion depth was determined to be larger than 4 nm. The intensity gradients for the C, Ga, and N atoms became more abrupt in the intermediate layer than those for the as-bonded and 700°C-annealed GaN/diamond heterointerfaces.

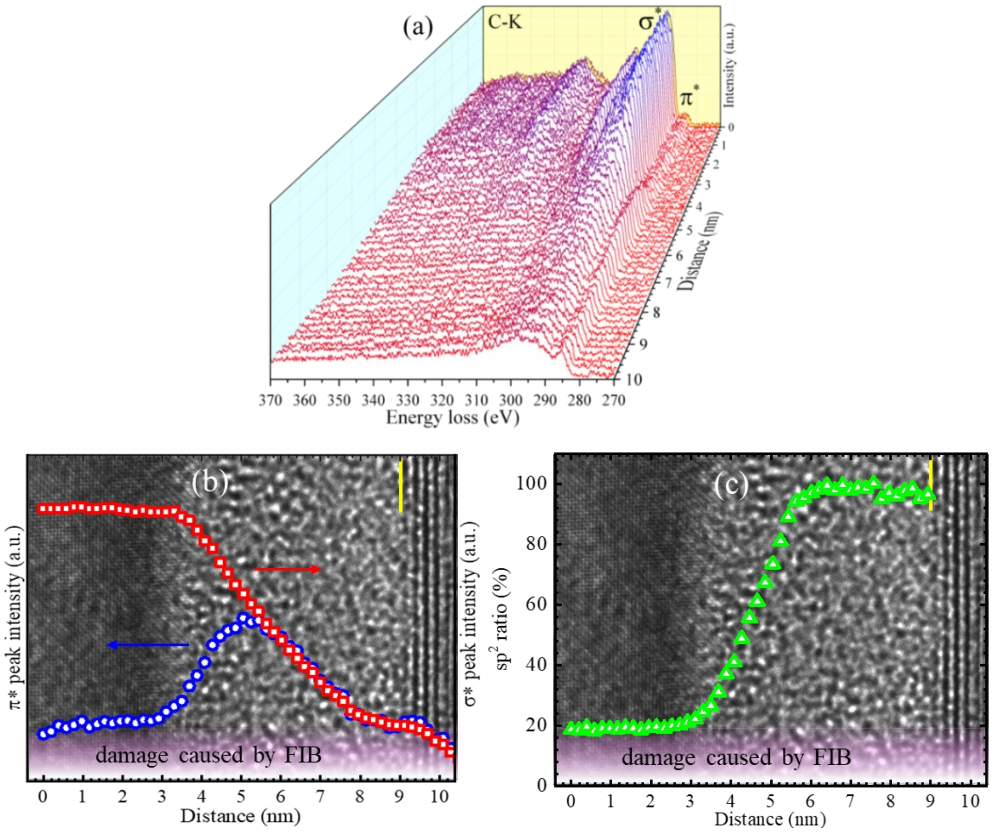

Figure 7. (a) *C-K* edge EELS spectra obtained from line scan across as-bonded GaN/diamond heterointerface. (b) π^* and σ^* peak intensities and (c) sp^2 ratio deduced from EELS spectra as a function of the scanned distance. The inset back in (b) and (c) shows TEM images of the as-bonded GaN/diamond heterointerface. The area filled with lavender in (b) shows the averaged π^* peak intensity of EELS spectra caused by FIB.

Figure 7(a)–(c) shows the *C-K* edge EELS line scan across an as-bonded GaN/diamond heterointerface with a step of 0.2 nm, π^* and σ^* peak intensities, and sp^2 ratio deduced from the EELS spectra as a function of the scanned distance. Two typical π^* and σ^* peaks for the carbon materials in EELS spectra were observed, located at approximately 285 and 292 eV, respectively. These π^* and σ^* peaks are typical for sp^2 trigonal coordination and sp^3 tetrahedral coordination carbon in graphite or amorphous carbon and diamond, respectively. Some small π^* peaks were observed in the EELS spectra of the diamond substrate adjacent to the intermediate layer, which we attribute to the surface damaged by FIB in the TEM sample fabrication process. A curve for the π^* peak relative intensity was observed, where the relative intensity change can be divided into two ranges: first, an increase in the range of 3–5.4 nm, and then, a decrease in the range of 5.4–10.4 nm. The σ^* peak relative intensity continually decreased in the range of 3–10.4 nm. The sp^2 ratios in Figure 7(b) were calculated by integrating the area of the π^* and σ^* peaks,

$$\mathrm{sp}^2(\%) = \frac{\pi^*/(\pi^*+\sigma^*)}{\pi^*_{amorphous\ carbon}/(\pi^*_{amorphous\ carbon}+\sigma^*_{amorphous\ carbon})} \times 100,$$

where $\pi^*_{\text{amorphous carbon}}$ and $\sigma^*_{\text{amorphous carbon}}$ were obtained by measuring a standard amorphous carbon material (see Figure S3 in the supplementary materials). The sp^2 ratio in the standard amorphous carbon material was calculated to be approximately 16 %. We found that the sp^2 ratio of the intermediate layer increased in the range of 2.7–6.2 nm and reached 100 % at 6.2 nm, after which it remained essentially the same in the range of 6.2–9 nm. Thus, the intermediate layer formed at the heterointerface can be divided into two parts: one part composed of amorphous carbon and diamond, and the other part an absolute amorphous carbon. Their thicknesses were determined to be approximately 3.5 and 2.8 nm, respectively.

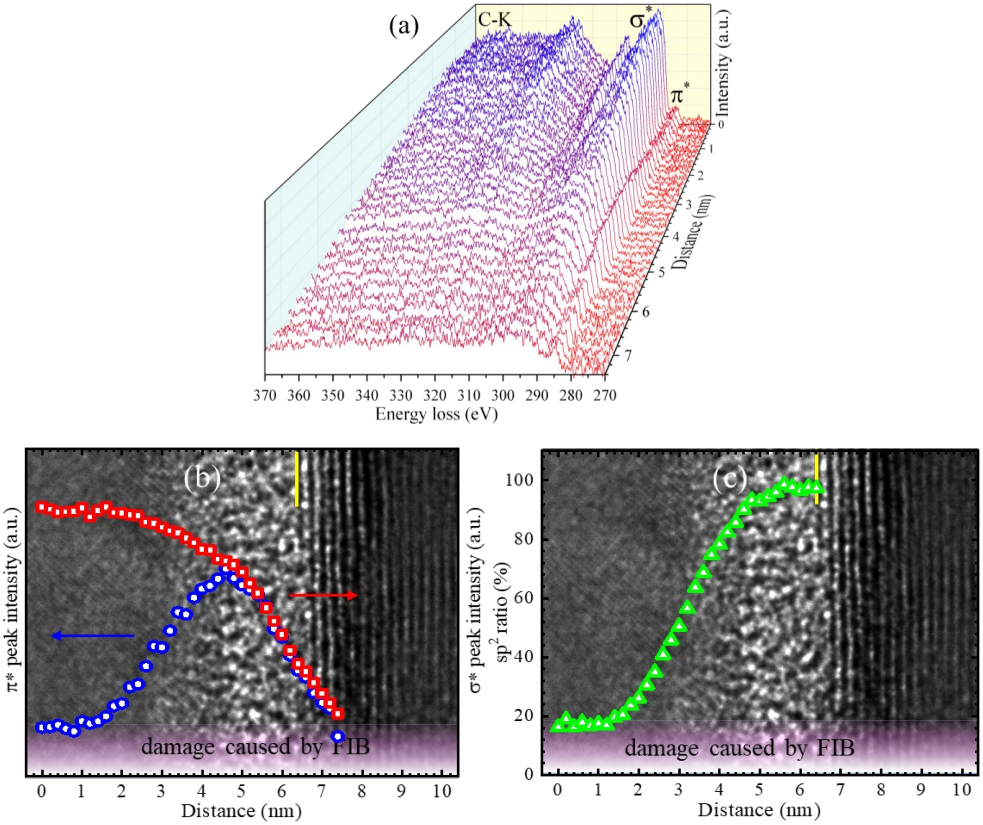

Figure 8. (a) *C-K* edge EELS spectra obtained from line scan across a 700 ℃-annealed GaN/diamond heterointerface. (b) π^* and σ^* peak intensities and (c) sp^2 ratio deduced from EELS spectra as a function of the scanned distance. The inset back in (b) and (c) shows TEM images of a 700 ℃-annealed GaN/diamond heterointerface. The area filled with lavender in (b) shows the averaged π^* peak intensity of EELS spectra caused by FIB.

Figure 8(a)–(c) shows the *C-K* edge EELS line scan across a 700 ℃-annealed GaN/diamond heterointerface, π^* and σ^* peak intensities, and sp^2 ratio deduced from the EELS spectra as a function of the scanned distance. A curve for the π^* peak relative intensity was also observed in the range of 1.6–7.4 nm, and the π^* peak relative intensity reached a peak at 4.8 nm, as shown

in Figure 8(b). The FWHM of the curve was smaller than that for the π^* peak relative intensity of the as-bonded GaN/diamond heterointerface. The σ^* peak relative intensity continually decreased in the range of 1.6–7.4 nm, similar to the as-bonded GaN/diamond heterointerface. The sp^2 ratio sharply increased in the range of 1.6–5.6 nm and reached 100 % at 5.6 nm, after which it remained the same in the range of 5.6–6.4 nm. Therefore, the thickness of the part composed of amorphous carbon and diamond was determined to be approximately 4.4 nm, and the thickness of the part composed of the absolute amorphous carbon was determined to be 0.8 nm.

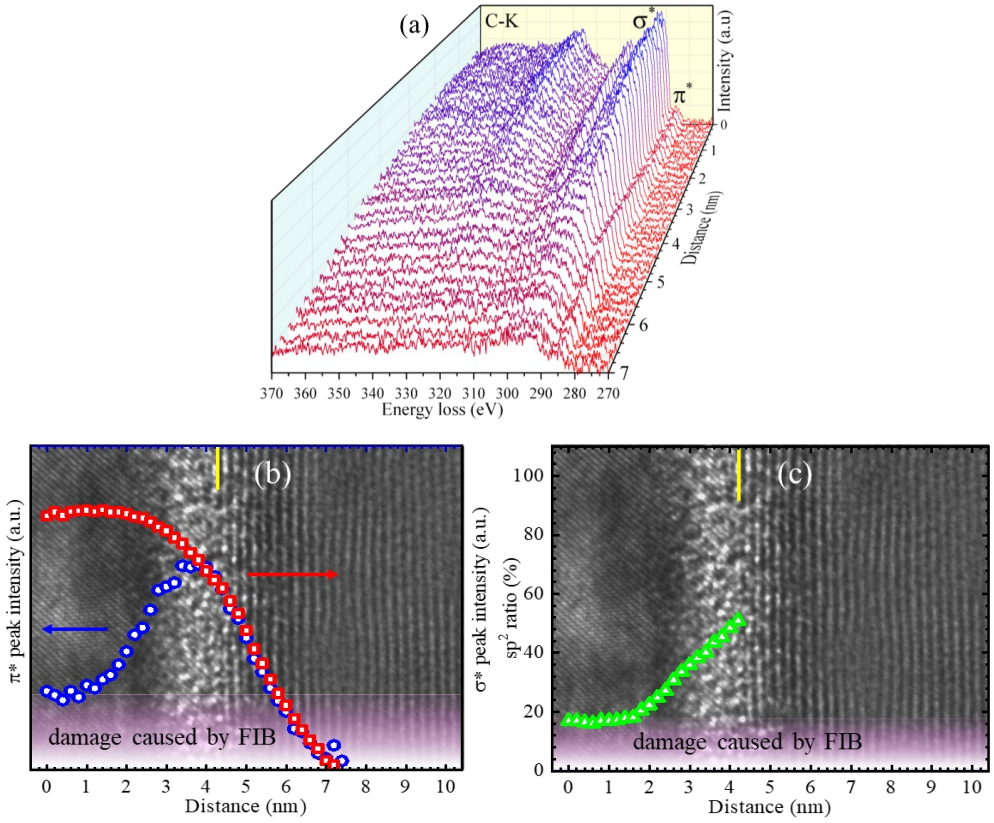

Figure 9. (a) *C-K* edge EELS spectra obtained from line scan across a 1000 ℃-annealed GaN/diamond heterointerface. (b) π^* and σ^* peak intensities. (c) sp^2 ratio deduced from EELS spectra as a function of the scanned distance. The inset back in (b) and (c) shows TEM images of a 1000 ℃-annealed GaN/diamond heterointerface. The area filled with lavender in (b) shows the averaged π^* peak intensity of EELS spectra caused by FIB.

Figure 9(a)–(c) shows the EELS line scan across a 1000 ℃-annealed GaN/diamond heterointerface, π^* and σ^* peak intensities, and sp^2 ratio deduced from the EELS spectra as a function of the scanned distance. We can see that the FWHM of the curve for the π^* peak relative intensity decreased as the annealing temperature increased, which was the smallest value among them. The reduction of the FWHM was in good agreement with the reduction of the intermediate layer thickness. The σ^* peak relative intensity was also found to continuity

decrease in the range of 1.4–7.4 nm, the same as the as-bonded and 700 °C-annealed GaN/diamond heterointerfaces. The sp^2 ratio gradually increased in the range of 1.4–4.2 nm and reached approximately 51 % at 4.2 nm. These results clearly show that the part composed of the absolute amorphous carbon was removed, and the thickness of the part composed of the amorphous carbon and diamond was approximately 2.6 nm. The actual sp^2 ratio of the intermediate layer was calculated to be between 0 and 34 % by subtracting the sp^2 ratio caused by FIB during the TEM sample fabrication process.

The compression stress in the as-bonded GaN/diamond heterointerface was larger than that of the GaN grown on Si (Figure 2(b)). We attribute this result to the high pressure (1 GPa) applied during the bonding process, which introduced compressive stress to the bonding interface. After annealing at 700 °C, the compressive stress in the heterointerface was relieved, as the component of the compressive stress caused by the applied pressure was removed by the post-annealing process. A similar result was reported for a Si/diamond interface fabricated by SAB.[31] At 500 °C, the compressive stress in the as-bonded and 700 °C-annealed GaN/diamond heterointerfaces increased to 0.81 and 0.74 GPa, which was larger than that (0.41 GPa) of the GaN grown on Si. This difference was mainly due to the thermal lattice expansion coefficient mismatch between diamond and GaN, which was larger than that between Si and GaN.[32-34] However, this compressive stress was smaller than that (1.1 GPa) of the GaN-on-diamond structure formed by the crystal growth of diamond on the GaN back side using a SiNx transition layer.[35] One possible explanation is that the atomic intermixing layer formed at the heterointerface acted as a buffer layer, reducing the elastic energy around the heterogeneous interface. A further important point is that this stress was significantly smaller than the mechanical strength (3.3 GPa) required for GaN fracture.

The fact that no lattice fringes were observed at the as-bonded GaN/diamond heterointerface indicates that the intermediate layer was an amorphous layer, the same as the Si/Si,[36,37] Si/SiC,[38] and Si/diamond[21] interfaces fabricated by SAB. However, this result is different from the Si/GaAs and GaAs/GaAs interfaces fabricated by SAB,[39,40] in which no amorphous layer was observed in the GaAs substrate adjacent to the bonding interface because the GaAs surface was not severely damaged by the Ar beam irradiation during the bonding process. The observed intensity gradients for C, Ga, and N atoms indicate that the amorphous layer was an atomic intermixing layer mainly composed of C, Ga, and N atoms. In addition, the π^* and σ^* peak intensities and the sp^2 ratio indicate that C atoms distributed in the atomic intermixing layer originated from the amorphous carbon and diamond. Therefore, it is difficult to determine whether the amorphous layer originated from the diamond, from GaN, or form both with the

density profiles and the carbon bonding states. To precisely determine the location of the heterointerface, we fabricated a GaN/GaN homointerface at room temperature under similar conditions and found that no amorphous layer was formed at the as-bonded GaN/GaN interface. We can therefore conclude that the amorphous layer originated entirely from the diamond. In addition, we hypothesize that the peak for O atom relative intensity should be located on the heterointerface (indicated by a solid yellow line in Figure 4(d)), as O atoms would locate on the Ar beam irradiated surfaces before bonding. Under this hypothesis, the exact location of the heterointerface can be determined.

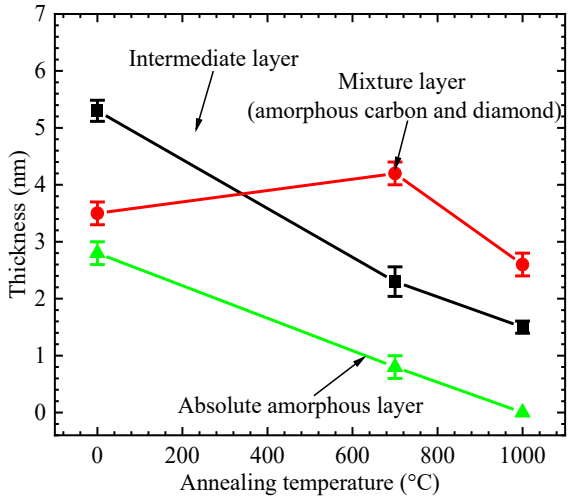

Figure 10. Intermediate layer, mixture layer composed of amorphous carbon and diamond, and absolute amorphous layer in the thickness change with annealing temperature.

We attribute the amorphous carbon of the intermediate layer to the covalent bond fracture of carbon atom in the diamond by the Ar beam irradiation in the bonding process. Similar results have been reported in laser-irradiated nanocrystalline diamond and low-energy ion-irradiated diamond.[41,42] The amorphous carbon of the intermediate layer formed at the interface should partially originate from the damage of focused ion beam (FIB) during TEM sample fabrication processes. It has been reported that the structural and compositional properties of interfaces fabricated by SAB were largely modified during FIB processes operated at room temperature, especially for wide band-gap materials.[37] Therefore, the inherent thickness of the intermediate layer should be more thin. Our results show that the intermediate layer was composed of a mixture layer made up of amorphous carbon and diamond, and an absolute amorphous carbon layer. The thicknesses of the mixture layer and the absolute amorphous carbon layer with annealing at different temperatures were obtained by referring to the heterointerface location and are shown in Figure 10. The thickness of the intermediate layer with different annealing temperatures is also added. We found that the thicknesses of the intermediate layer and the absolute amorphous carbon layer decreased with increasing annealing temperature. After

annealing at 1000 ℃, the thickness of the intermediate layer was reduced from 5.3 to 1.5 nm and the absolute amorphous carbon layer completely disappeared. Meanwhile, the thickness of the mixture layer composed of amorphous carbon and diamond increased after annealing at 700 ℃, and then decreased when annealing temperature increased to 1000 ℃.

For the thickness behavior of the absolute amorphous carbon layer with annealing temperature, there are two possible explanations, namely that the carbon atoms of the absolute amorphous carbon layer completely diffused into the GaN and the amorphous carbon was converted into diamond after annealing. Density profiles of C, Ga, and N atoms across the as-bonded, 700 ℃-annealed, and 1000 ℃-annealed interfaces were shown in Figure 11(a)-(c), respectively. The density profiles for C atoms diffused into the GaN were fitted by a one-dimensional diffusion equation: C_0 erfc [x/(2L)] (the dotted black curves in Figure 11 (a)-(c)) with an error function of the distance x from the interface and a diffusion constant L.[40] The densities of C atoms in the as-bonded, 700 ℃-annealed, and 1000 ℃-annealed interfaces were obtained to be approximately 12.1×10^{21}, 27.8×10^{21}, 18.5×10^{21} cm^{-3}, respectively. The diffusion lengthes of C atoms in the GaN adjacent to the as-bonded, 700 ℃-annealed, and 1000 ℃-annealed interfaces were estimated to be approximately 1.3, 1.6, and 2.0 nm, repectively. The estimated diffusion lenght of C atoms in the GaN of the 1000 ℃-annealed interface is in agreement with the reported result for carbon diffusion in GaN at 1000 ℃.[43] The densities of sp^2 and sp^3 bonded carbon atoms in the diamond adjacent to the as-bonded, 700 ℃-annealed, and 1000 ℃-annealed interfaces were estimated to be approximately 98.5×10^{21} and 3.5×10^{21}, 97.6×10^{21} and 4.9×10^{21}, and 51.1×10^{21} and 87.6×10^{21} cm^{-3}, respectively (Figure 11(d)-(f)). All observed results such as the density and diffusion lenght of C atoms in the GaN adjacent to the 1000 ℃-annealed interface, the density and thickness variations of sp^2 bonded carbon atoms in the absoluate amrphous carbon layer with annealing temperture, indicate that the disiappearance of the absoluate amrphous carbon layer due to the diffusion of C atoms is unlikely to occur because a longer diffuion lenght is requied for the diffusion of all C atoms in the absoluate amrphous carbon layer. Furthermore, the density increase of sp^3 bonded carbon atoms in the diamond adjacent to the interfaces with anealing temperature and the thickness variation of the mixture layer made up of amorphous carbon and diamond are in good agreement with the coversion features.

In the conversion process, it should start from the diamond side and the diamond of the mixture layer acts as a seed crystal. Similar properties have been obtained for laser-irradiated amorphous carbon,[44] in which the amorphous carbon was converted into diamond by nanosecond laser irradiation at room temperature. The conversion of the amorphous carbon into

diamond is consistent with the solid-phase transformation of a metastable amorphous material into a crystal.[45] The activation energy required for the transmormation is supplied in the form of thermal energy by increasing the temperature of the material. The solid-phase transformation of an amorphous Si even can be performed at a low temperature of 200 °C.[46] Similar properties were observed in SAB-fabricated GaAs/Si, GaP/GaAs, and GaSb/GaInP interfaces.[47-49] The diffusion of Ga and N atoms is much more likely to occur in amorphous carbon than in diamond due to the former's low atomic density.[50] No diffusion of Ga or N atoms into the diamond substrate adjacent to the intermediate layer was observed even after annealing at 1000 °C, while the C atom diffused into the GaN after annealing at 700 °C. The diffusion length of the Ga and N atoms became shorter as the annealing temperature increased, so the density gradients for the C, Ga, and N atoms became much more abrupt in the intermediate layer. Meanwhile, the O atom distributed in the heterointerface further diffused into the GaN substrate with the increase of annealing temperature, and finally reached at the background level after annealing at 1000 °C.

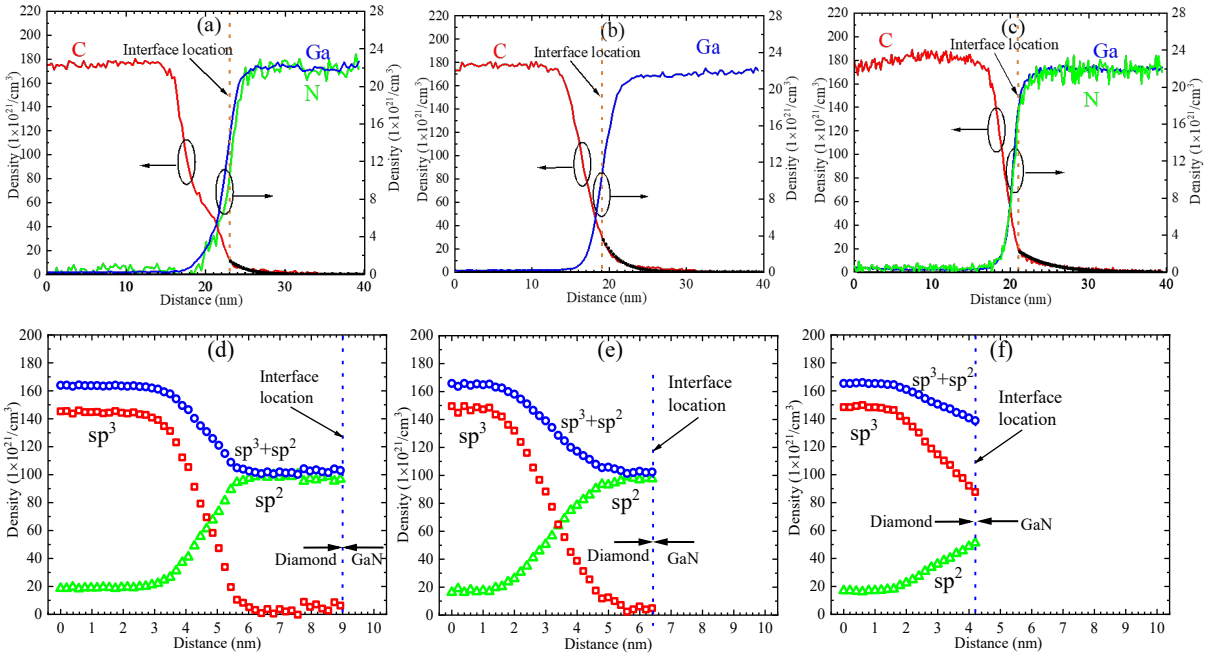

Figure 11. Density profiles of C, Ga, and N atoms (red, blue, and green, respectively) across the (a) as-bonded, (b) 700 °C-annealed, and (c) 1000 °C-annealed GaN/diamond heterointerfaces obtained by EDX. Density profiles of sp^2, sp^3, and sp^2+sp^3 bonded carbon atoms (green, red, and blue, respectively) in the diamond adjacent to the (d) as-bonded, (e) 700 °C-annealed, and (f) 1000 °C-annealed GaN/diamond heterointerfaces obtained by sp^2 ratio.

The intermediate layer formed at the as-bonded GaN/diamond heterointerface seems to have had an extremely small effect on the TBR, as the TBR originated mainly from the heterogeneous interface.[51,52] Reports have shown that the TBR of an as-bonded Cu/diamond interface with a 4.5-nm-thick intermediate layer is in good agreement with the value calculated

by the phonon diffuse mismatch model.[53] Furthermore, the TBR of as-bonded Si/Si interface fabricated by SAB was found to have a thermal resistance equivalent to that of micrometer-thick bulk Si.[54] For the GaN-on-diamond structures developed by crystal growth and low-temperature bonding technologies, the introduction of a transition layer or adhesion layer is essential, but this will result in a double heterogeneous interface. The TBR value of the GaN-on-diamond structures formed by the chemical vapor deposition of diamond on GaN[9,12,52,55] was much larger than the value calculated by the phonon diffuse mismatch model.[12] The large TBR value is attributed to the double heterogeneous interface. Meanwhile, the deposited diamond near the interface was extremely low in the crystal quality, which resulted in a low thermal conductivity that counteracted the advantage of the high thermal conductivity of the diamond substrate. Recently, the room-temperature bonding of GaN and single-crystal diamond using amorphous Si as an adhesion layer has been reported,[13] in which the TBR value was found to be many times larger than the value calculated by the phonon diffuse mismatch model. As with the GaN-on-diamond structure formed by crystal growth, the double heterogeneous interface still existed in the GaN-on-diamond structure formed by room temperature bonding. Although the total heat dissipation property of GaN-on-diamond devices has made excellent progress due to the use of single-crystal diamond substrate, high-density Fe atoms are induced in the amorphous Si layer during the bonding process, which results in a parasitic capacitance in the GaN-on-diamond devices during high frequency operation due to a high electrical conductivity of the adhesion layer. This parasitic capacitance limits the maximum input frequency of the GaN-on-diamond devices.

For the 1000 ℃-annealed GaN/diamond heterointerface, lattice fringes and the sp^2 ratio lower than 35 % observed in the intermediate layer indicate that the intermediate layer was a crystal defect layer of diamond. No voids and no mechanical cracks were observed at the heterointerface. Although the crystal defect diamond layer formed at the interface may affect the carriers transport properties across the heterointerfaces, which can be optimized by controlling the SAB condition. The optimized heterointerfaces have been applied to various functional devices, such as high-efficiency tandem solar cells with a low interface electrical resistance,[56,57] high-power semiconductor lasers with a low interface thermal resistance,[58] and high-efficiency heterojunction diodes with a very small reverse-bias current.[59,60] As the GaN/diamond heterointerface uses a high-quality diamond substrate and no adhesion layer, an extremely small TBR can be expected, which is very advantageous for heat dissipation of the devices. The C atoms that diffuse into the GaN can be used as a dopant to compensate for the nitrogen vacancies in the GaN to increase the electrical resistance of the GaN layer, which is

very beneficial for enhancing the breakdown voltage of GaN-based devices.[61] In addition, if the insulative diamond substrate is replaced with a p-type diamond substrate, which is very useful for developing n-GaN/i-GaN/p-diamond heterojunction diodes with a high breakdown voltage and an excellent heat dissipation. In short, the GaN/diamond heterointerface will play an important role in the performance enhancement of GaN-based devices and the development of devices with novel functions such as deep ultraviolet light-emitting diodes[62,63] and millimeter-wave devices.[64]

3. Conclusion

In this paper, we reported the fabrication of a GaN/diamond heterointerface through the direct bonding of GaN and diamond substrate using the SAB technique at room temperature. An intermediate layer with a thickness of approximately 5.3 nm was formed at the as-bonded GaN/diamond heterointerface. The intermediate layer was a mixture layer composed of amorphous carbon and diamond in which Ga and N atoms were distributed. The intermediate layer thickness decreased with increasing annealing temperature due to the direct conversion of amorphous carbon into diamond. The distribution area of Ga and N atoms also decreased with the reduction of the intermediate layer thickness. After annealing at 1000 ℃, the thickness of the intermediate layer was decreased to approximately 1.5 nm, where lattice fringes were observed. This indicates that the intermediate layer can be completely removed by optimizing the annealing process. The intensity gradients for C, Ga, and N atoms showed an abrupt GaN/diamond heterointerface. A compressive stress of 0.1 GPa existed in the GaN/diamond heterointerface, which increased to 0.74 GPa at 500 ℃. However, this compressive stress was significantly smaller than that of the GaN-on-diamond structures formed by the crystal growth. These results demonstrate that the GaN/diamond heterointerface has a high mechanical stability and can withstand the harsh devices fabrication process.

4. Experimental Section

GaN epitaxial layers grown on Si (111) and CVD-synthesized diamond substrates were used for direct bonding experiments. The thickness and size of the diamond was 450 μm and 4.5 mm × 4.5 mm, respectively. The GaN epitaxial substrate was composed of a 1000-nm-thick GaN and a 100-nm-thick AlN buffer layer grown on a Si (100) substrate. Before bonding, the diamond surface was treated by a mechanical polishing technique to obtain a surface with better flatness. Atomic force microscope (AFM) measurements of the averaged roughness (Ra) of the diamond surface before and after polishing showed that it was 1.609 and 0.277 nm, respectively.

The surface Ra of the GaN layers grown on Si was 0.396 nm. AFM images of the diamond before and after polishing and the GaN surfaces are shown in Figure 12(a), (b), and (c), respectively. The diamond substrates were cleaned with the sulfuric acid-hydrogen peroxide mixture (H_2SO_4: H_2O_2 = 4:1) at 80 °C for 10 min, rinsed with deionized water for 3 min, and dried under N_2 flow. The GaN epitaxial substrates were cleaned with acetone and isopropyl alcohol in an ultrasonic bath for 300 s and dried under N_2 flow. After cleaning, the diamond and GaN epitaxial substrates were placed in a vacuum facility for direct bonding. The surfaces of the diamond and GaN were simultaneously irradiated by an Ar fast atom beam (FAB) in a vacuum pressure of 5.0×10^{-7} Pa. The Ar FAB irradiation voltage and current was 1.6 kV and 1.6 mA, respectively. As soon as the irradiation process was finished, the diamond and GaN were brought into contact by applying a load of 1 GPa for 60 s at room temperature. After bonding, the Si substrates were removed by mechanical polishing and wet etching processes.

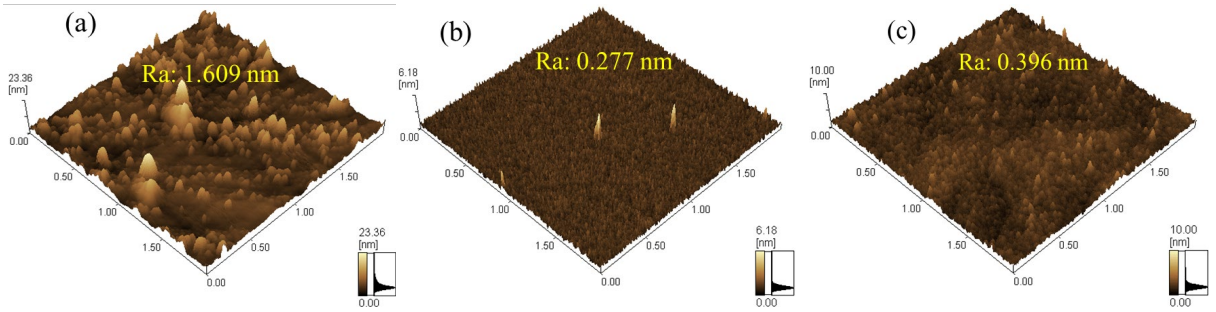

Figure 12. AFM images of diamond (a) before and (b) after polishing, and (c) GaN surfaces.

The stress state of GaN in the GaN/diamond bonded sample was evaluated by micro-Raman spectroscopy in a vacuum condition at different heating temperatures. Raman spectroscopy measurements were also performed on the GaN-on-Si and a stress-free GaN substrate for comparison. The heating process was conducted on a high-temperature heating stage with a temperature error of ±1 ℃. A 488-nm Ar laser was used as the excitation source. The structure and chemical composition of the GaN/diamond heterointerface without and with annealing at 700 and 1000 ℃ for 1 min were analyzed by TEM and energy-dispersive x-ray spectroscopy (EDX) under STEM with a JEOL JEM-2200FS analytical microscope. The bonding states of carbon atoms near the GaN/diamond heterointerface with annealing at various temperatures were investigated by EELS under STEM. Carbon K-shell edge spectra were taken between 270 and 370 eV at an acceleration voltage of 200 KV. The TEM samples were prepared by the focused ion beam (FIB) technique (Helios NanoLab600i; Thermo Fisher Scientific) at room temperature.

Supporting Information

Supporting Infromation is available from the Wiley Online Library.

Acknowledgements

This work was supported by the “Research and development of high thermal stability interface by direct bonding of diamond” project in the Feasibility Study Program of New Energy and Industrial Technology Development Organization (NEDO) (contract number: 19101242-0), JSPS KAKENHI Grant Number JP20K04581, and the Osaka City University (OCU) Strategic Research Grant 2020 for top basic research. The fabrication of the TEM samples was performed at The Oarai Center and at the Laboratory of Alpha-Ray Emitters in IMR under the Inter-University Cooperative Research in IMR of Tohoku University (NO. 18M0045 and 19M0037). A part of this work was supported by Kyoto University Nano Technology Hub in the "Nanotechnology Platform Project" sponsored by the Ministry of Education, Culture, Sports, Science and Technology (MEXT), Japan. GaN single-crystal substrate grown by HVPE used for the stress-free GaN was provided by Sciocs Co. Ltd., Japan.

Conflict of Interest

The authors declare no conflict of interest.

References

[1] J. Isberg, J. Hammersberg, E. Johansson, T. Wikström, D. J. Twitchen, A. J. Whitehead, S. E. Core, G. A. Scarsbrook, *Science* **2002**, *297*, 1670.

[2] F. Nava, C. Canali, C. Jacoboni, L. Reggiani, S. F. Kozlov, *Solid State Commun*. **1980**, *33*, 475.

[3] H. Umezawa, T. Matsumoto, S. Shikata, *IEEE Electron Device Lett*. **2014**, *35*, 1112.

[4] H. Umezawa, M. Nagase, Y. Kato, S. Shikata, *Diamond Relat. Mater.* **2012**, *24*, 201.

[5] T. Liu, Y. Kong, L. Wu, H. Guo, J. Zhou, C. Kong, T. Chen, *IEEE Electron Device Lett*. **2017**, *38*, 1417.

[6] J. Cho, Z. Li, E. Bozorg-Grayeli, T. Kodama, D. Francis, F. Ejeckam, F. Faili, M. Asheghi, K. E. Goodson, *IEEE Trans. Compon. Packag. Manuf. Technol.* **2013**, *3*, 79.

[7] H. Sun, J. W. Pomeroy, R. B. Simon, D. Francis, F. Faili, D. J. Twitchen, M. Kuball, *IEEE Electron Device Lett*. **2016**, *37*, 621.

[8] P. Chao, K. Chu, C. Creamer, J. Diaz, T. Yurovchak, M. Shur, R. Kallaher, C. McGray, G. D. Via, J. D. Blevins, *IEEE Trans. Electron Devices* **2015**, *62*, 3658.

[9] Y. Zhou, J. Anaya, J. Pomeroy, H. Sun, X. Gu, A. Xie, E. Beam, M. Becker, T. A. Grotjohn, C. Lee, M. Kuball, *ACS Appl. Mater. Interfaces* **2019**, *9*, 34416.

[10] A. Siddique, R. Ahmed, J. Anderson, M. Nazari, L. Yates, S. Graham, M. Holtz, E. L. Piner, *ACS Appl. Electron. Mater.* **2019,** *1*, 1387.

[11] S. Mandal, J. Cuenca, F. Massabuau, C. Yuan, H. Bland, J. W. Pomeroy, D. Wallis, T. Batten, D. Morgan, R. Oliver, M. Kuball, O. A. Williams, *ACS Appl. Mater. Interfaces* **2019**, *11*, 40826.

[12] H. Sun, R. B. Simon, J. W. Pomeroy, D. Francis, F. Faili, D. J. Twitchen, M. Kuball, *Appl. Phys. Lett*. **2015**, *106*, 111906.

[13] Z. Cheng, F. Mu, L. Yates, T. Suga, S. Graham, *ACS Appl. Mater. Interfaces* **2020**, *12*, 8376.

[14] J. Kim, J. Lee, J. Kim, R. K. Singh, P. Jawali, G. Subhash, H. Lee, A. Arjunan, *Scr. Mater.* **2018**, *142*, 138.

[15] K. Wang, K. Ruan, W. Hu, S. Wu, H. Wang, *Scr. Mater.* **2020**, *174*, 87.

[16] D. Francis, F. Faili, D. Babic, F. Ejeckam, A. Nurmikko, H. D. Maris, *Diamond Relat. Mater.* **2010**, *19*, 229.

[17] T. Matsumae, Y. Kurashima, H. Umezawa, K. Tanaka, T. Ito, H. Watanabe, H. Takagi, *Appl. Phys. Lett.* **2020**, *116*, 141602.

[18] T. Matsumae, Y. Kurashima, H. Umezawa, H. Tagagi, *Jpn. J. Appl. Phys*. **2020**, *59*, SBBA01.

[19] J. Liang, Y. Nakamura, Y. Ohno, Y. Shimizu, Y. Nagai, H. Wang, N. Shigekawa, *Funct. Diam*. **2021**, *1,* 110.

[20] T. Matsumae, M. Fengwen, S. Fukumoto, M. Hayase, Y. Kurashima, E. Higurashi, H. Takagi, T. Suga, *J. Alloys Compd*. **2021**, *852*, 156933.

[21] J. Liang, S. Masuya, M. Kasu, N. Shigekawa, *Appl. Phys. Lett.* **2017**, *110*, 111603.

[22] J. Liang, S. Masuya, S. Kim, T. Oishi, M. Kasu, N. Shigekawa, *Appl. Phys. Express* **2019,** *12*, 016501.

[23] J. Liang, Y. Nakamura, T. Zhan, Y. Ohno, Y. Shimizu, K. Katayama, T. Watanabe, H. Yoshida, Y. Nagai, H. Wang, M. Kasu, N. Shigekawa, *Diamond Relat. Mater.* **2021**, *111*, 108207.

[24] J. M. Wagner, F. Bechstedt, *Phys. Status Solidi B*, **2002**, *234*, 965.

[25] K. Torii, M. Ono, T. Sota, T. T. Azuhata, S. F. Chichibu, S. Nakamura, *Phys. Rev. B* **2000**, *62*, 10861.

[26] M. Amilusik, T. Sochacki, M. Fijalkowski, B. Lucznik, M. Iwinska, A. Sidor, H. Teisseyre, J. Domagala, I. Grzegory, M. Bockowski, *Jpn. J. Appl. Phys*. **2019**, *58*, SC1030.

[27] J. C. Gallagher, T. J. Anderson, L. E. Luna, A. D. Koehler, J. K. Hite, N. A. Mahadik, K. D. Hobart, F. J. Kub, *J. Crys. Growth* **2019**, *506*, 178.

[28] K. Karch, I. M. Wagner, F. Bechstedt, *Phys. Rev. B* **1998**, *57*, 7043.

[29] R. Rornari, M. Bosi, D. Bersani, G. Attolini, P. P. Lottici, C. Pelosi, *Semicond. Sci. Technol.* **2001**, *16*, 776.

[30] L. Qi, Y. Xu, Z. Li, E. Zhao, S. Yang, B. Cao, J. Zhang, J. Wang, K. Xu, *Maer. Lett.* **2016**, *185*, 315.

[31] J. Liang, Y. Zhou, S. Masuya, F. Gucmann, M. Singh, J. Pomeroy, S. Kim, M. Kuball, M. Kasu, N. Shigekawa. *Diamond Relat. Mater.* **2019**, *93*, 187.

[32] K. Haruna, H. Maeta, K. Ohashi, T. Koike, *Jpn. J. Appl. Phys.* **1992**, *31*, 2527.

[33] M. Leszczynski, T. Suski, H. Teisseyre, P. Perlin, I. Grzegory, J. Jun, S. Porowski, T. D. Moustakas, *J. Appl. Phys.* **1994**, *76*, 4909.

[34] H. Watanabe, N. Yamada, M. Okaji, *Int. J. Thermophys.* **2004**, *25*, 221.

[35] D. Liu, H. Sun, J. W. Pomeroy, D. Francis, F. Faili, D. J. Twitchen, M. Kuball, *Appl. Phys. Lett.* **2015**, *107*, 251902.

[36] J. Liang, T. Miyazaki, M. Morimoto, S. Nishida, N. Shigekawa, *J. Appl. Phys.* **2013**, *114*, No. 183703.

[37] Y. Ohno, H. Yoshida, N. Kamituchi, R. Aso, S. Takeda, Y. Shimizu, Y. Nagai, J. Liang, N. Shigekawa, *Jpn. J. Appl. Phys*. **2020**, *59*, SBBB05.

[38] J. Liang, S. Nishida, M. Arai, N. Shigekawa, *Appl. Phys. Lett*. **2014**, *104*, 161604.

[39] Y. Ohno, H. Yoshida, S. Takeda, J. Liang, N. Shigekawa, *Jpn. J. Appl. Phys.* **2018**, 57, 02BA01.

[40] Y. Ohno, J. Liang, N. Shigeka, H. Yoshida, S. Takeda, R. Miyagawa, Y. Shimizu, Y. Nagai, *Appl. Phys. Sur.* **2020**, *525*, 146610.

[41] A. Zkria, E. Abukakr, M. Egiza, A. Haque, J. Narayan, T. Yoshitake, *Appl. Phys. Express* **2020**, *13*, 105503.

[42] R. Reinke, G. Francz, P. Oelhafen, J. Ullmann, *Phys. Rev. B* **1996**, *54*, 7067.

[43] T. Kimura, S. Ootomo, T. Nomura, S. Yoshida, T. Hashizume, *Jpn. J. Appl. Phys*. **2007**, *46*, L224.

[44] J. Narayan, A. Bhaumik, *Appl. Phys. Lett. Mater*. **2015**, *3*, 100702.

[45] L. Stoch, I. Waclawska, *High Temp. Mater. Process.* **1994**, *13*, 181.

[46] M. M. R. Howlader, F. Zhang, *Thin Solid Films* **2010**, *519*, 804.

[47] S. Yamajo, S. Yoon, J. Liang, H. Sodabanlu, K. Watanabe, M. Sugiyama, A. Yasui, E. Ikenaga, N. Shigekawa, *Appl. Surf. Sci.* **2019**, *473*, 627.

[48] M. M. R. Howlader, T. Suga, F. Zhang, T. H. Lee, M. J. Kim, *Electrochem. Solid-State Lett.* **2010**, *13*, H61.

[49] F. Predan, A. Kovács, J. Ohlmann, D. Lackner, R. E. Dunin-Borkowski, F. Dimroth, W. Jäger, *J. Appl. Phys*. **2017**, *122*, 13507.

[50] Z. Zeng, L. Yang, Q. Zeng, H. Lou, H. Sheng, J. Wen, D. J. Miller, Y. Meng, W. Yang, W. J. Mao, H. Mao, *Nature Communications* **2017**, *8*, 322.

[51] J. W. Pomeroy, M. Bernardoni, D. C. Dumka, D. M. Fanning, M. Kuball, *Appl. Phys. Lett.* **2014**, 104, 083513.

[52] L. Yates, J. Anderson, X. Gu, C. Lee, T. Bai, M. Mecklenburg, T. Aoki, M. S. Goorsky, M. Kuball, E. L. Piner, S. Graham, *ACS Appl. Mater. Interfaces* **2018**, *10*, 24302.

[53] J. Liang, Y. Ohno, Y. Yamashita, Y. Shimizu, S. Kanda, N. Kamiuchi, S. Kim, K. Koji, Y. Nagai, M. Kasu, N. Shigekawa, *ACS Appl. Nano Mater*. **2020**, *3*, 2455.

[54] M. Sakata, T. Oyake, J. Maire, M. Nomura, E. Higurashi, J. Shiomi, *Appl. Phys. Lett.* **2015**, 106, 081603.

[55] Y. Zhou, R. Ramaneti, J. Anaya, S. Korneychuk, J. Derluyn, H. Sun, J. Pomeroy, J. Verbeeck, K. Haenen, M. Kuball, *Appl. Phys. Lett*. **2017**, *111*, 041901.

[56] K. Derendorf, S. Essig, E. Oliva, V. Klinger, T. Roesener, S. P. Philipps, J. Benick, M. Hermle, M. Schachtner, G. Siefer, W. Jager, F. Dimroth, *IEEE J. Photovolt.* **2013**, *3*, 1423.

[57] N. Shigekawa, J. Liang, R. Onitsuka, T. Agui, H. Juso, T. Takamoto, *Jpn. J. Appl. Phys*. **2015**, *54*, 08KE03.

[58] E. Higurashi, K. Okumura, K. Nakasuji, T. Suga, *Jpn. J. Appl. Phys.* **2015**, *54*, 030207.

[59] J. Liang, S. Nishida, M. Arai, N. Shigekawa, *Appl. Phys. Lett.* **2014**, *104*, 161604.

[60] J. Liang, T. Miyazaki, M. Morimoto, S. Nishida, N. Watanabe, N. Shigekawa, *Appl. Phys.Express* **2013**, *6*, 021801.

[61] N. Remesh, N. Mohan, S. Raghavan, R. Muralidharan, D. N. Nath, *IEEE Trans. Electron Devices* **2020**, 99, 1.

[62] C. R. Miskys, J. A. Garrido, C. E. Nebel, M. Hermann, O. Ambacher, M. Eickhoff, M. Stutzmann, *Appl. Phys. Lett*. **2003**, *82*, 290.

[63] K. Hirama, Y. Taniyasu, M. Kasu, *Appl. Phys. Lett*. **2011**, *98*, 011908.

[64] A. Acharyya, S. Banerjee, J. P. Banerjee, *J. Semiconductors* **2014**, 35, 034005.